Deformable image registration between pathological images and MR image via an optical macro image

Takashi Ohnishi[a,*], **Yuka Nakamura**[b], **Toru Tanaka**[b], **Takuya Tanaka**[b], **Noriaki Hashimoto**[a], **Hideaki Haneishi**[a], **Tracy T. Batchelor**[c,d], **Elizabeth R. Gerstner**[c,d], **Jennie W. Taylor**[c,d,1], **Matija Snuderl**[e], and **Yukako Yagi**[d,f]

[a]Center for Frontier Medical Engineering, Chiba University, 1-33, Yayoi-cho, Inage-ku, Chiba 263-8522, Japan

[b]Graduate School of Engineering, Chiba University, Japan

[c]Massachusetts General Hospital Cancer Center, Boston, MA 02144, USA

[d]Harvard Medical School, Boston, MA 02215, USA

[e]New York University Langone Medical Center, New York, NY 10016, USA

[f]Massachusetts General Hospital Pathology Imaging and Communication Technology (PICT) Center, Boston, MA 02214, USA

Abstract

Computed tomography (CT) and magnetic resonance (MR) imaging have been widely used for visualizing the inside of the human body. However, in many cases, pathological diagnosis is conducted through a biopsy or resection of an organ to evaluate the condition of tissues as definitive diagnosis. To provide more advanced information onto CT or MR image, it is necessary to reveal the relationship between tissue information and image signals. We propose a registration scheme for a set of PT images of divided specimens and a 3D-MR image by reference to an optical macro image (OM image) captured by an optical camera. We conducted a fundamental study using a resected human brain after the death of a brain cancer patient. We constructed two kinds of registration processes using the OM image as the base for both registrations to make conversion parameters between the PT and MR images. The aligned PT images had shapes similar to the OM image. On the other hand, the extracted cross-sectional MR image was similar to the OM image. From these resultant conversion parameters, the corresponding region on the PT image could be searched and displayed when an arbitrary pixel on the MR image was selected. The relationship between the PT and MR images of the whole brain can be analyzed using the proposed method. We confirmed that same regions between the PT and MR images could be searched and displayed using resultant information obtained by the proposed method. In terms of the accuracy of proposed method, the TREs were 0.56 ± 0.39 mm and 0.87 ± 0.42 mm. We can analyze the relationship between tissue information and MR signals using the proposed method.

*Corresponding author. t-ohnishi@chiba-u.jp (T. Ohnishi).
[1]J.W.T. is currently affiliated with the University of California, San Francisco, San Francisco, CA 94143, USA.

1. Introduction

Computed tomography (CT) and magnetic resonance (MR) imaging have been widely used to visualize the inside of the human body. However, in many cases, a definitive diagnosis cannot be conducted from such images. A pathological diagnosis is thus conducted through a biopsy or resection of an organ to evaluate the condition of tissues. To obtain more advanced information from a CT or MR image, it is necessary to reveal the relationship between tissue information and image signals. For this purpose, the methodologies of multi-modal and multi-scale image analysis have been developed [1–28]. In this regard, pathological (PT) images have been used to obtain the tissue information. However, PT specimens are generally deformed during image-acquisition processes. It is thus important to develop highly accurate image registration, involving deformation correction for PT specimens. Many prior studies have formulated methods of establishing the relationship between PT and MR images [1–28].

Most of the studies cited above examined the prostate or brain. Among these studies, several developed methods can be used for images of the brains of small animals, such as rats, mice, and rabbits [15,16,25,29], while others employed methods may be applied to a small part of the human brain [11,22]. Ideally, a whole human organ should be analyzed with the PT and MR images. However, if an ordinary microtome is used to obtain the PT images, the human organ must be divided into several block sections before the thin-slicing process; this is because such a large organ cannot be thinly sliced using an ordinary machine.

One study [1] developed a large-scale microtome to produce large specimens without requiring the blocking process. However, the thin-sliced specimens obtained using this machine are limited to a thickness of over 20 μm. To conduct a fine relationship analysis, thinner specimens with thicknesses less than 10 μm are favorable because some tissue information cannot be obtained from thicker specimens.

If an organ is divided into several blocks, deformation occurs in each blocked organ. Previous studies [4,23,30] have developed reconstruction platforms, involving a graphical user interface, to process PT images from several divided specimens and create an entire PT image. The platforms developed by Chappelow's group [4] and Toth's group [23] prepare a whole PT image using feature points selected by the operator. However, it connects only the PT images; it does not use a reference image. Thus, the connected PT images generated using this system cannot be directly compared with MR images. Hashimoto's group also developed a platform to create a whole PT image [30]. A gross optical image was used as a reference image to align the PT images. The system could automatically create the whole PT image. However, since the image alignment was achieved by some simple affine transformations, the resultant whole PT image tended to have several unnatural gaps.

In the present study, we propose a registration scheme for a set of PT images of divided specimens and a three-dimensional (3D) MR image by reference to an optical macro (OM) image captured by an optical camera. We conducted a fundamental study using a human brain removed after death from a brain-tumor patient. An outline of this study and the image acquisition process is shown in Fig. 1. First, a 3D-MR image is obtained from the resected organ. The organ is then divided into several thick gross sections, each with a thickness of about 5 mm. The OM image of each gross section is captured by the camera. After recording such OM images, the gross sections are divided into several blocks and pathological specimens are made on slide glasses and digitized as PT images. This process is common in histopathology and the thickness of pathological specimens is around 5 μm. We constructed two kinds of registration processes using the OM image as a common reference in both registrations to obtain parameters for the conversion between PT and MR images. The first registration produces parameters for the conversion between the PT and OM image. The second registration produces parameters for the conversion between the OM image and MR image. The coordinates of the PT and MR images are reciprocally converted with the resultant parameters for the conversion obtained from the proposed method. The proposed method was applied to image sets acquired from a resected human brain.

2. Materials and methods

Fig. 2 shows the flow of the proposed method. The method consists of two kinds of image registration. The first one produces parameters for the conversion between the PT images of the specimen and the OM image of the gross section. The second produces parameters for the conversion between the OM images of the gross section and the 3D-MR image of the whole brain. Using the conversion parameters from the two registrations, we are able to identify the corresponding regions between the PT images and MR image.

2.1. OM–PT image registration

An OM image is used as a reference image to determine the conversion parameters. Because the distribution of the pixel values is very different between PT and OM images, intensity-based image registration methods are not appropriate in this regard. We therefore used the thin-plate spline (TPS) method [31], which is a feature-point-based non-rigid registration technique. The TPS method requires pairs of the corresponding feature points selected from the reference image and floating image. The feature points selected from the OM image are defined as target points; the feature points selected from the PT images are defined as control points. It is noted that each pair of a target point and control point must be marked on the correct corresponding point. The conversion parameters are generated from coordinates of the feature points. The translation of the control points to the target points is

$$\begin{bmatrix} \mathbf{K} & \boldsymbol{P} \\ \boldsymbol{P}^T & \mathbf{0} \end{bmatrix} \begin{bmatrix} \mathbf{W} \\ \boldsymbol{A} \end{bmatrix} = \begin{bmatrix} \mathbf{V} \\ \mathbf{0} \end{bmatrix}, \quad (1)$$

where

$$\mathbf{P} = \begin{bmatrix} 1 & x_1 & y_1 \\ 1 & x_2 & y_2 \\ \vdots & \vdots & \vdots \\ 1 & x_n & y_n \end{bmatrix},$$

(2)

$$\mathbf{V} = \begin{bmatrix} x'_1 & y'_1 \\ \vdots & \vdots \\ x'_n & y'_n \end{bmatrix},$$

(3)

$$\mathbf{A} = \begin{bmatrix} a_{x1} & a_{y1} \\ a_{x2} & a_{y2} \\ a_{x3} & a_{y3} \end{bmatrix},$$

(4)

$$\mathbf{W} = \begin{bmatrix} w_{x1} & w_{y1} \\ \vdots & \vdots \\ w_{xn} & w_{yn} \end{bmatrix}.$$

(5)

Here, $\mathbf{P}$ is a matrix including coordinates of the control points, and $\mathbf{V}$ is a matrix including coordinates of the target points. The matrices $\mathbf{A}$ and $\mathbf{W}$ are the parameters of the affine transform and weighting factor, respectively. These are the conversion parameters to be generated in this registration. n indicates the number of control points. $\mathbf{K}$ is a matrix that has radial basis functions $U(r)$ as non-diagonal elements:

$$\mathbf{K} = \begin{bmatrix} 0 & U(r_{12}) & \cdots & U(r_{1n}) \\ U(r_{21}) & 0 & \cdots & U(r_{2n}) \\ \vdots & \vdots & \ddots & \vdots \\ U(r_{n1}) & U(r_{n2}) & \cdots & 0 \end{bmatrix},$$

(6)

$$U(r) = r^2 \ln r^2.$$

(7)

Here, r_{ij} denotes the pairwise distance between a target point and control point and is calculated as

$$r_{ij} = \sqrt{(x_j - x_i)^2 + (y_j - y_i)^2}. \quad (8)$$

To obtain **A** and **W**, Eq. (1) is rewritten as

$$\left[\begin{array}{c} \mathbf{W} \\ \mathbf{A} \end{array} \right] = \left[\begin{array}{cc} \mathbf{K} & \boldsymbol{P} \\ \boldsymbol{P}^T & \mathbf{0} \end{array} \right]^{-1} \left[\begin{array}{c} \mathbf{V} \\ \mathbf{0} \end{array} \right]. \quad (9)$$

After calculating the affine factor matrix **A** and weighting factor matrix **W**, any coordinates of the pathological images can be translated according to

$$x' = a_{x1} + a_{x2}x + a_{x3}y + \sum_{i=1}^{n} w_{xi} U(r), \quad (10)$$

$$y' = a_{y1} + a_{y2}x + a_{y3}y + \sum_{i=1}^{n} w_{yi} U(r). \quad (11)$$

2.2. Connecting PT images

The process of connecting PT images is optionally performed after the OM–PT image registration. The OM–PT image registration cannot completely eliminate blank and overlapping regions from aligned PT images; this is because the TPS method does not conduct complex deformation with a small number of pairs of feature points. If specimens can be obtained by thinly slicing at the same depth with assumed and the consecutiveness of slices can be assumed, this process can be applied to PT images. The flow of the connection process is shown in Fig. 3. Some pairs of control points are selected from a pair of PT images. The target points are set at the midpoint of the corresponding control points, and the PT images are deformed using the TPS method. Control points are then iteratively added at the midpoint of control points on the PT image from the previous step. This step is iterated a specified number of times.

2.3. OM–MR image registration

The parameters of conversion between an OM image and 3D-MR image are obtained using a simple affine registration. Here, a two-dimensional MR image similar to the OM image is extracted from the 3D-MR image. The similarity between the OM image and extracted MR image is measured by conditional mutual information (CMI) [32] as follows:

$$CMI = H(\mathbf{A}|\mathbf{X}) + H(\mathbf{B}|\mathbf{X}) - H(\mathbf{A}, \mathbf{B}|\mathbf{X})$$
$$= \sum_X p(x) \sum_B \sum_A p(a,b|x) \ln\left(\frac{p(a,b|x)}{p(a|x)p(b|x)}\right), \quad (12)$$

$$p_A(a|x) = \frac{p_A(a,x)}{p_A(x)}. \quad (13)$$

Here, $\mathbf{A}$ and $\mathbf{B}$ denote distributions of the pixel values of each image, and $\mathbf{X}$ denotes the spatial coordinates. $H(|)$ represents the conditional entropy. $p()$ and $p(|)$ are the probability density and conditional probability density, respectively. The conditional probability density is calculated using Eq. (13). CMI uses spatial binning for standard mutual information (SMI), which means that CMI evaluates the sum of local MI values with a weight based on the probability density of each spatial bin. Thus, CMI can robustly evaluate the similarity between images better than SMI even if a bias of the intensity fields exists on the MR image.

Affine parameters for the OM image are optimized by the artificial bee colony algorithm (ABCA) [33] and Powell–Brent algorithm (PBA) [34]. Here, there are nine affine parameters, namely translation parameters t_i, rotation parameters r_i, and scale parameters s_i for each direction $i = \{X, Y, Z\}$. The ABCA is an intelligent global search algorithm. It initially spreads many sets of candidate parameters in a solution space and searches for an optimum solution. The PBA is a classic local search algorithm that searches for a solution with only one set of candidate parameters. The ABCA is used to coarsely search the whole 3D-MR image and identify a cross-sectional MR image that is similar to the OM image. The PBA is then used to find a cross-sectional MR image that is more similar to the OM image.

3. Experiments and results

3.1. Data acquisition

We used an image dataset acquired from the brain resected from a patient who had glioblastoma. The T2*-weighted image of the whole brain was acquired using a 7T MR scanner (Magnetom 7T, Siemens, Erlangen, Germany). The image size and number of slices were 870×640 pixels and 950 slices, respectively. The in-plane pixel size was 0.2×0.2 mm^2, and the slice thickness was 0.2 mm. The brain was fixed with formalin for a week. The fixed brain was divided into 17 gross sections at 5 mm intervals, and each gross section was captured by an optical camera with RGB color channels as an OM image. The image size and pixel size of the OM images were 2000×1500 pixels and 0.056×0.056 mm^2, respectively. Here, the side surfaces of the specimens in the OM image were manually eliminated because these regions were unnecessary for registration. Each gross section was then divided into several block sections, and each block section was sliced thinly at 5 μm intervals. All sections were stained with hematoxylin–eosin and captured using a whole slide scanner (Nano Zoomer 2.0-HT, Hamamatsu Photonics K.K., Hamamatsu, Japan). The pixel size of the PT images was 0.5×0.5 μm^2.

3.2. Results of OM–PT image registration with connection

The gross section of the OM image was divided into left and right parts, as shown in Figs. 4 a and 5 a. We manually selected 51 pairs of corresponding feature points from the OM and PT images of the left part, as shown in Fig. 4b, c. We also manually selected 47 pairs of corresponding feature points for the right part, as shown in Fig. 5b, c. The results of OM–PT registration are shown in Figs. 4 d and 5 d. All the aligned PT images were similar to the OM image. However, we observed blank regions and areas of insufficient deformation correction. We therefore attempted connection of the PT images as described in the section "Connecting PT images" above. We set the number of iteration times of the connection process to three. Figs. 4 e and 5 e show the results of that connection process. To visualize the correspondence between the OM and connected PT images, superimposed images of the connected PT image and edge of the OM image are shown in Figs. 4 f and 5 f. The shapes of the connected PT images of both the right and left parts indicated strong correspondence with the edges of the OM images.

We tested another dataset of the gross section, as shown in Figs. 6 and 7. We manually selected 38 and 44 pairs of the corresponding feature points from the OM image and PT images of each part. As with the dataset of the above gross section, we still observed blank regions in the aligned PT images of both parts, as shown in Figs. 6 d and 7 d. Such blank regions were eliminated after the connection process, as indicated in Figs. 6 e and 7 e. The shapes of both connected PT images were similar to those of the OM images. The results obtained with the dataset of the other gross sections were similar, and we judged them to be successful.

3.3. Results of OM–MR image registration

The ABCA was terminated after 2500 iterations; there were 10 candidate sets of conversion parameters, and the parameter searching was limited to 10 times. In this OM–MR image registration, the green channel of the OM image was used for CMI calculation because the contrast of the green channel was higher than that of the red and blue channels. Typical results of OM–MR registration are shown in Fig. 8. The optimized cross-sectional MR image is shown in Fig. 8b. From a comparison of Fig. 8a and b, we noted that the extracted cross-sectional MR image was very similar to the OM image. The results of another gross section are shown in Fig. 9. A cross-sectional MR image similar to the OM image was extracted just as in Fig. 8. As for the other gross sections, all the extracted cross-sectional MR images were similar to the corresponding OM images.

3.4. Identifying the corresponding region—a demonstration

We attempted to identify the corresponding region of the PT and MR images using conversion parameters calculated from the OM–PT and OM–MR image registrations. If the conversion parameters are correctly obtained, the corresponding regions of the PT and MR images can be observed. We assumed that an operator selected an arbitrary region on the extracted cross-sectional MR image shown in Fig. 10a. The corresponding region of the PT image was then calculated with the resultant conversion parameters. Fig. 10a, b shows the cross-sectional MR image and connected PT image with a square for the region selected by the operator. The result suggests that the corresponding region on the PT image can be

displayed when an arbitrary pixel on the MR image is selected. The proposed method converts the coordinates; thus, an enlarged region of the original PT image for the corresponding region can be searched and displayed without spatial distortion as a result of the OM–PT image registration and connection process, as shown in Fig. 10c, d. Fig. 11 presents the cross-sectional MR image and connected PT image of the second gross section. In a visual assessment, we confirmed that the similarity between these images was also high.

Target registration error (TRE) was used to measure the accuracy of registration between the MR and PT images. We defined TRE as the average distance between arbitrary landmarks on extracted cross-sectional MR image $\mathbf{p}_i$ and corresponding landmarks on PT images after registration $\mathbf{q}_i$:

$$TRE = \sum_{i=1}^{N} \|\mathbf{p}_i - \mathbf{q}_i\|_2 / N. \tag{14}$$

Here, i and N represent a landmark number and the number of landmarks. In this study, we manually selected 10 pairs of landmarks (with the exception of feature points used in registrations) from each pair of cross-sectional MR and PT images. The TREs of the two gross sections were 0.56 ± 0.39 mm and 0.87 ± 0.42 mm. Thus, these TREs were equal to 2.8 and 4.2 pixels in the MR image space or about 1100 and 1700 pixels in the PT image space.

4. Discussion

In this study, we developed two kinds of image registration methods of determining the parameters for the conversion between PT images and a 3D-MR image. The OM–PT image registration was based on a TPS method. Experimentally, we found that the aligned PT images of both the right and left brain had shapes similar to those of the OM images. From observations of the inner structure of the connected PT image, the corresponding white matters and gray matters were naturally connected without excessive deformation. However, the image quality of the aligned and connected PT images depended on the selection of control and target points in the image registration and connection processes. Furthermore, such point selection was an onerous manual operation. Thus, future improvements will need an automatic point selection algorithm and pair-making algorithm.

In terms of OM–MR image registration, the extracted cross-sectional MR images had a shape very similar to that of the OM images. These results substantiated the effectiveness of the proposed method. We assumed that a simple affine registration could represent the difference between an OM image and MR image. However, affine registration can correct only global distortion on a flat surface linearly. If the cut plane of the gross section is a curved surface or there is local distortion, affine registration cannot produce suitable parameters for the conversion between the OM and MR images. To deal with these problems, a specific sectioning slicer able to cut the brain with a completely planar surface and negligibly small local distortion is necessary, as proposed by Drew et al. [7]. Furthermore, a non-rigid registration method, such as TPS, should be implemented for OM–

MR image registration. As for the optimization method of OM–MR registration, even if the initial parameters were set to the same parameters for every gross section, the ABCA produced suboptimum conversion parameters; the PBA obtained better conversion parameters. This indicates the robustness of the proposed OM–MR image registration and obviates the onerous operation.

A critical problem with both OM–PT and OM–MR image registration is the effect of the side surface of the specimens in the OM image. Since the blocks of the specimens are thick, not only the top surface of the block but also its sides are captured. These side regions are unnecessary for OM–PT and OM–MR image registration because the cross-sectional MR image to be extracted and the PT images to be connected are ideally a perfect plane or curved surface. To improve the accuracy and robustness of both OM–PT and OM–MR image registration, only the top surface of the specimen should be captured; other regions should be eliminated from the OM image. In this study, we manually eliminated such excess regions. However, manually excluding such regions is burdensome and impedes smooth analysis. It is thus necessary to introduce an automated elimination method. One solution could be to obtain the 3D shape of the block using optical techniques [35] and to extract the top surface region.

In terms of the accuracy of proposed method, the TREs of the two gross sections were 0.56 ± 0.39 mm and 0.87 ± 0.42 mm. Choe's group [5] and Goubran's group [11] reported registration methods with accuracies of 0.32 ± 0.28 mm and 0.40 ± 1.8 mm, respectively. Both of their accuracies were superior to those in the present study. However, the objects examined in previous studies were small, such as the brain of an owl monkey or parts of organs, and the initial error was also low, such as 4.5 ± 0.28 mm. When the object is large, the difficulty of image registration increases. One study, whose object was a fully resected larynx [28], reported accuracy of 2.6 ± 2.5 mm. In the present study, even when the object was as large as 100 mm in diameter and divided into a number of blocks, the proposed method provided highly accurate conversion parameters and well-matching results.

This study has some limitations in terms of the used MR sequence and MR scanner. In this paper, the T2*-weighted MR image of an ex-vivo brain obtained by a 7 T MR scanner was used for the image registration. To complete the whole study of this scheme, however, as shown in Fig. 1, 3D-MRI of an in-vivo organ needs to be registered and analyzed. At present, commonly used MR scanner for human subjects has magnetic field intensities of 3 T or 1.5 T. There are also various pulse sequences in such MRI acquisition. The differences of the magnetic field intensity and imaging sequence lead to the difference of image quality and consequently may bring a different performance from this paper. This issue must be carefully clarified hereafter.

5. Conclusions

Toward establishing a relationship between MR signals and tissue information, we proposed a method of image registration for pathological and 3D-MR images using an optical macro image. To confirm the effectiveness of the proposed method, we conducted an experiment with a resected human brain, removed after the death of a brain-tumor patient. We confirmed

that the same regions in pathological and MR images could be searched and displayed using the information obtained with the proposed method. Thus, with our method, we can analyze the relationship between tissue information and MR signals.

Acknowledgments

References

1. Amunts K, Lepage C, Borgeat L, Mohlberg H, Dickscheid T, Rousseau ME, Bludau S, Bazin PL, Lewis LB, Peusquens AMO, Shah NJ, Lippert T, Zilles K, Evans AC. Bigbrain: an ultrahigh-resolution 3D human brain model. Science. 2013; 21:1472–1475.

2. Budde MD, Kim JH, Liang HF, Schmidt RE, Russell JH, Cross AH, Song SK. Toward accurate diagnosis of white matter pathology using diffusion tensor imaging. Magn Reson Med. 2007; 57:688–695. [PubMed: 17390365]

3. Ceritoglu C, Wang L, Selemon LD, Csemansky JG, Miller MI, Ratnanather JT. Large deformation diffeomorphic metric mapping registration of reconstructed 3D histological section images and in vivo MR images. Front Hum Neurosci. 2010; 4:1–11. [PubMed: 20204154]

4. Chappelow J, Tomaszewski JE, Feldman M, Shih N, Madabhushi A. Histostitcher: an interacttive program for accurate and rapid reconstruction of digitized whole histological sections from tissue fragments. Comput Med Imaging Graph. 2011; 35:557–567. [PubMed: 21397459]

5. Choe AS, Gao Y, Li X, Compthon KB, Stepniewska I, Anderson AW. Accuracy of image registration between MRI and light microscopy in the ex vivo brain. Magn Reson Imaging. 2011; 29:683–692. [PubMed: 21546191]

6. Dauguet J, Delzescaux T, Conde F, Mangin JF, Ayache N, Hantraye P, Frouin V. Three-dimensional reconstruction of stained histological slices and 3D non-linear registration with in-vivo MRI for whole baboon brain. J Neurosci Methods. 2007; 164:191–204. [PubMed: 17560659]

7. Drew B, Jones EC, Reinsberg S, Yung AC, Goldenberg SL, Koziowski P. Device for sectioning prostatectomy specimens to facilitate comparison between histology and in vivo MRI. J Magn Reson Imaging. 2010; 32:992–996. [PubMed: 20882632]

8. Eriksson SH, Free SL, Thom M, Harkness W, Sisodiya SM, Duncan JS. Reliable registration of Preoperative MRI with histopathology after temporal lobe resections. Epilepsia. 2005; 46:1646–1653. [PubMed: 16190938]

9. Gefen S, Kiryati N, Nissanov J. Atlas based indexing of brain sections via 2-D to 3-D image registration. IEEE Trans Biomed Eng. 2008; 55:147–156. [PubMed: 18232356]

10. Goubran M, Crukley C, Ribaupierre S, Peters TM, Khan AR. Image registration of ex-vivo MRI to sparsely sectioned histology of hippocampal and neocortical temporal lobe specimens. Neuroimage. 2013; 83:770–781. [PubMed: 23891884]

11. Goubran M, Ribaupirre S, Hammond RR, Currie C, Burneo JG, Parrent AG, Peters TM, Khan AR. Registration of in-vivo to ex-vivo MRI of surgically resected specimens: a pipeline for histology to in-vivo registration. J Neurosci Methods. 2015; 41:53–65.

12. Groenedaal G, Moman MR, Korporaal JG, Diest PJ, Vulpen M, Philippens MEP, van der Heide UA. Validation of functional imaging with pathology for tumor delineation in the prostate. Radiother Oncol. 2010; 94:145–150. [PubMed: 20116116]

13. Kyriacou SK, Davatzikos C, Zinreich SJ, Bryan RN. Nonlinear elastic registration of brain images with tumor pathology using a biomechanical model. IEEE Trans Med Imaging. 1999; 18:580–592. [PubMed: 10504092]

14. Lebenberg J, Herard AS, Dubois A, Dauguet J, Frouin V, Dhenain M, Hantraye P, Delzescaux T. Validation of MRI-based 3D digital atlas registration with histological and autoradiographicumes: an anatomofunctional transgenic mouse brain imaging study. Neuroimage. 2010; 51:1037–1046. [PubMed: 20226256]

15. Li G, Nikolova S, Bartha R. Registration of in vivo magnetic resonance T1-weighted brain images to triphenyltetrazolium chloride stained sections in small animals. J Neurosci Methods. 2006; 156:368–375. [PubMed: 16682080]

16. Liu Y, Sajja BR, Uberti MG, Gendelman HE, Kielian T, Boska MD. Landmark optimization using local curvature for point-based nonlinear rodent brain image registration. Int J Biomed Imaging. 2012; 2012:1–8.

17. Nir G, Sahebjavaher RS, Kozlowski P, Chang SD, Jones EC, Goldenberg SL, Salcudean SE. Registration of whole-mount histology and volumetric imaging of the prostate using particle filtering. IEEE Trans Med Imaging. 2014; 33:1601–1613. [PubMed: 24771576]

18. Osechinskiy S, Kruggel F. Slice-to-volume nonrigid registration of histological sections to MR images of the human brain. Anat Res Int. 2011; 2011:1–17.

19. Ou, Y.; She, D.; Feldman, M.; Tomaszewski, J.; Davatzikos, C. Non-rigid registration between histological and MR images of the prostate: a joint segmentation and registration framework. IEEE CVPR Workshops; 2009; p. 125-132.

20. Park H, Piert MR, Khan A, Shah R, Hussain H, Siddiqui J, Chenevert TL, Meyer CR. Registration methodology for histological sections and in vivo imaging of human prostate. Acad Radiol. 2008; 15:1027–1039. [PubMed: 18620123]

21. Schormann T, Dabringhaus A, Zilles K. Statistics of deformations in histology and application to improved alignment with MRI. IEEE Trans Med Imaging. 1995; 14:25–35. [PubMed: 18215807]

22. Singh M, Rajagopalan A, Kim TS, Hwang D, Chui H, Zhang XL, Lee AY, Zarow C. Co-registration of in vivo human MRI brain images to postmortem histological microscopic images. Int J Imaging Syst Technol. 2008; 18:325–335. [PubMed: 19169415]

23. Toth RJ, Shih N, Tomaszewski JE, Feldman MD, Kutter O, Yu DN, Paulus JC, Paladini G, Madabhushi A. Histostitcher™: an informatics software platform for reconstructing whole-mount prostate histology using the extensible imaging platform framework. J Pathol Inform. 2014; 5:1–9. [PubMed: 24672736]

24. Xiao G, Bloch BN, Chappelow J, Genega EM, Rofsky NM, Lenkinski RE, Tomaszewski J, Feldman MD, Rosen M, Madabhushi A. Determining histology-MRI slice correspondences for defining MRI-based disease signatures of prostate cancer. Comput Med Imaging Graph. 2011; 35:568–578. [PubMed: 21255974]

25. Yang Z, Richards K, Kurniawan ND, Petrou S, Reutens DC. MRI-guided volume reconstructtion of mouse brain from histological sections. J Neurosci Methods. 2012; 211:210–217. [PubMed: 22981936]

26. Yelnik J, Bardinet E, Dormont D, Malandain G, Ourselin S, Tande D, Karachi C, Ayache N, Cornu P, Agid Y. A three-dimensional, histological and deformable atlas of the human basal ganglia. I. Atlas construction based on immunohistochemical and MRI data. Neuroimage. 2007; 34:618–638. [PubMed: 17110133]

27. Zhan Y, Ou Y, Feldman M, Tomaszeweski J, Davazikos C, Shen D. Registering histologic and MR images of prostate for image-based cancer detection. Acad Radiol. 2007; 14:1367–1381. [PubMed: 17964460]

28. Magalhaes JC, Kasperts N, Kooij N, Berg CAT, Terhaard CHJ, Raaijmakers CPJ, Philippens MEP. Validation of imaging with pathology in laryngeal cancer: accuracy of the registration methodology. Int J Rad Oncol Biol Phys. 2012; 82:e289–e298.

29. Meyer CR, Moffat BA, Kuszpit K, Bland PL, Chenevert TL, Rehemtulla A, Ross BD. A methodology for registration of a histological slide and in vivo MRI volume based on optimizing mutual information. Mol Imaging. 2006; 5:16–23. [PubMed: 16779966]

30. Hashimoto N, Bautista PA, Haneishi H, Snuderl M, Yagi Y. Development of a 2D image reconstruction and viewing system for histological images from multiple tissue blocks: towards high-resolution whole-organ 3D histological images. Patholobiology. 2016; 83:127–139.

31. Bookstein FD. Principle Warps: thin-plate splines and decomposition of deformations. IEEE Trans Pattern Anal Mach Intell. 1989; 11:567–585.

32. Loeckx D, Slagmolen P, Maes F, Vandermeulen D, Suetens P. Nonrigid image registration using conditional mutual information. IEEE Trans Med Imaging. 2010; 29:19–29. [PubMed: 19447700]

33. Karaboga D, Basturk B. Artificial bee colony optimization Algorithm for solving constrained optimization problems. Found Fuzzy Log Soft Comput. 2007; 4529:789–798.

34. Press, WH.; Teukolsky, SA.; Vetterling, WT.; Flanner, BP. Numerical Recipes in C. 2. Cambridge University Press; 2002. p. 412-419.

35. Zhang Q, Su X, Xiang L, Sun X. 3-D shape measurement based on complementary Gray-code light. Opt Lasers Eng. 2012; 50:574–579.
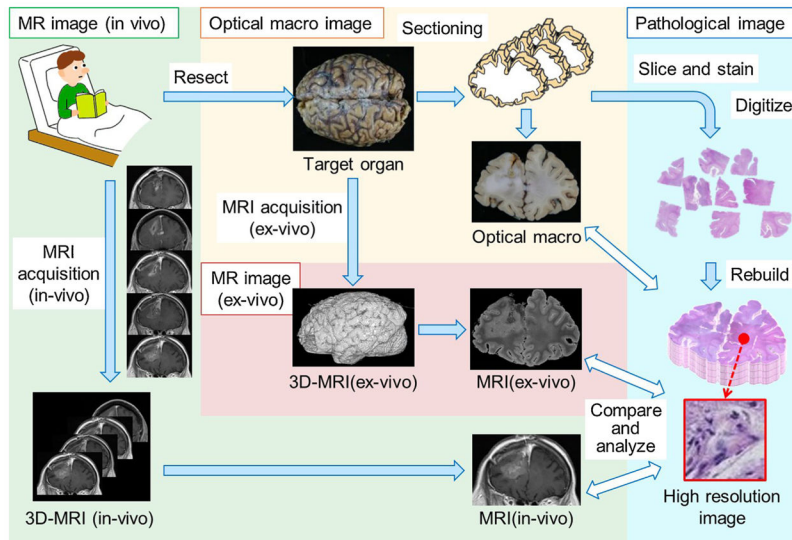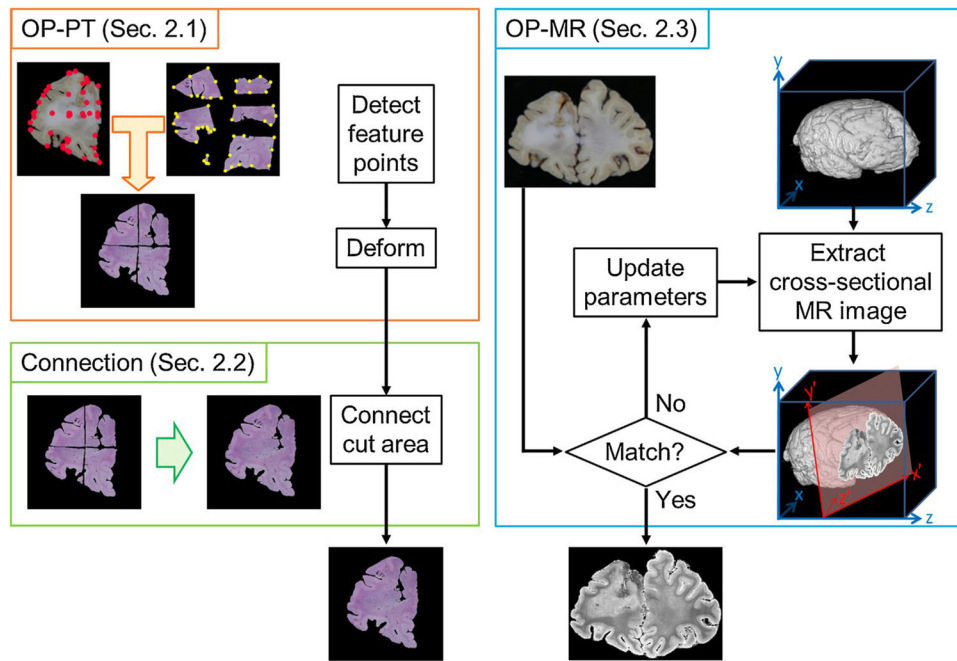
Fig. 1.
Study overview.

Fig. 2.
Flow for obtaining parameters of conversion between PT images and the 3D-MR image.
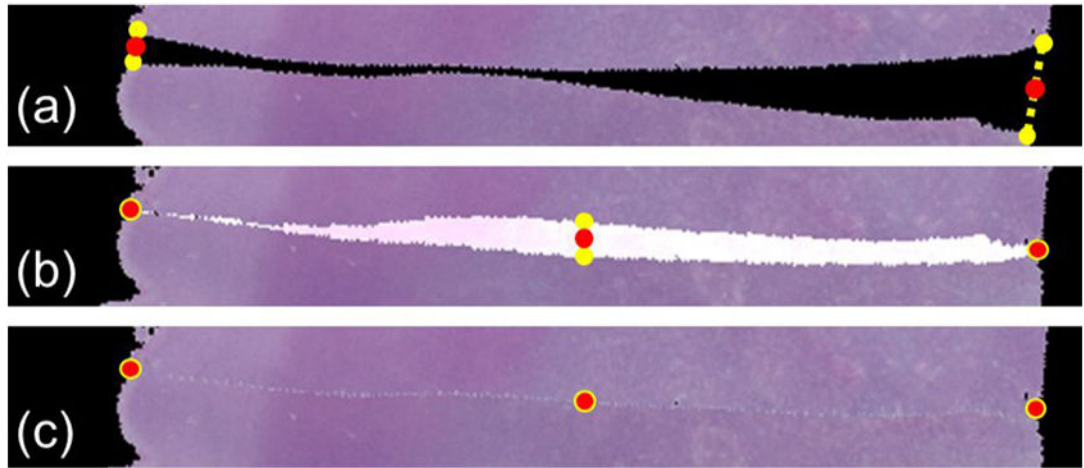
Fig. 3.
Schematic illustration of the connection of PT images. (a) First step; (b) second step; (c) result of the connection process. Red dots represent target points; yellow dots represent control points. The black area is a blank region; the white area is an overlapping region. (For interpretation of the references to colour in this figure legend, the reader is referred to the web version of this article.)
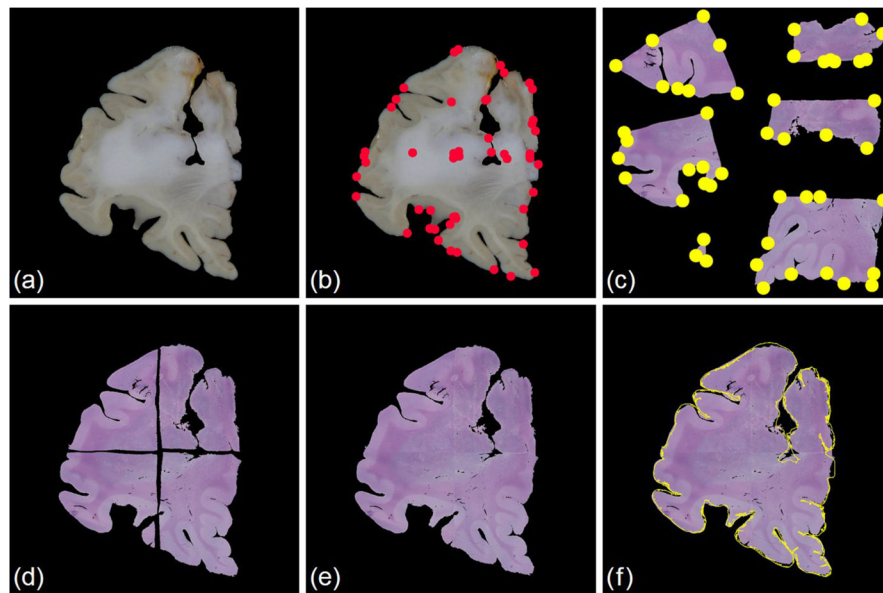
Fig. 4.
Results of OM–PT image registration with the connection step for the left part of the first gross section. (a) OM image of the left part of the first gross section; (b) OM image with selected target points; (c) PT images with selected control points before OM–PT image registration; (d) aligned PT images after OM–PT image registration; (e) connected PT image; (f) superimposed image with (e) and edge of (a). Red dots represent target points; yellow dots represent control points. (For interpretation of the references to colour in this figure legend, the reader is referred to the web version of this article.)
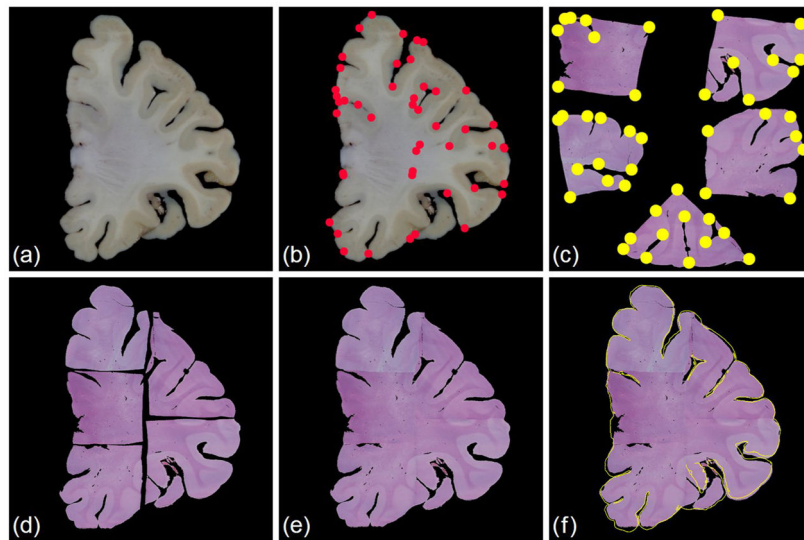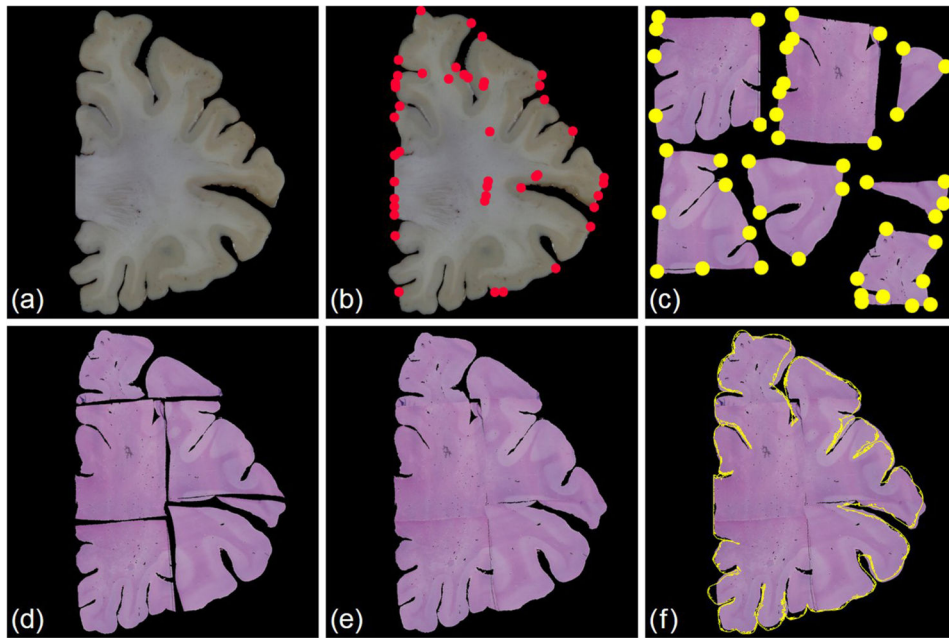
Fig. 5.
Results of OM–PT image registration with the connection step for the right part of the first gross section. (a) OM image of the right part of the first gross section; (b) OM image with selected target points; (c) PT images with selected control points before OM–PT image registration; (d) aligned PT images after OM–PT image registration; (e) connected PT image; (f) superimposed image with (e) and edge of (a). Red dots represent target points; yellow dots represent control points. (For interpretation of the references to colour in this figure legend, the reader is referred to the web version of this article.)
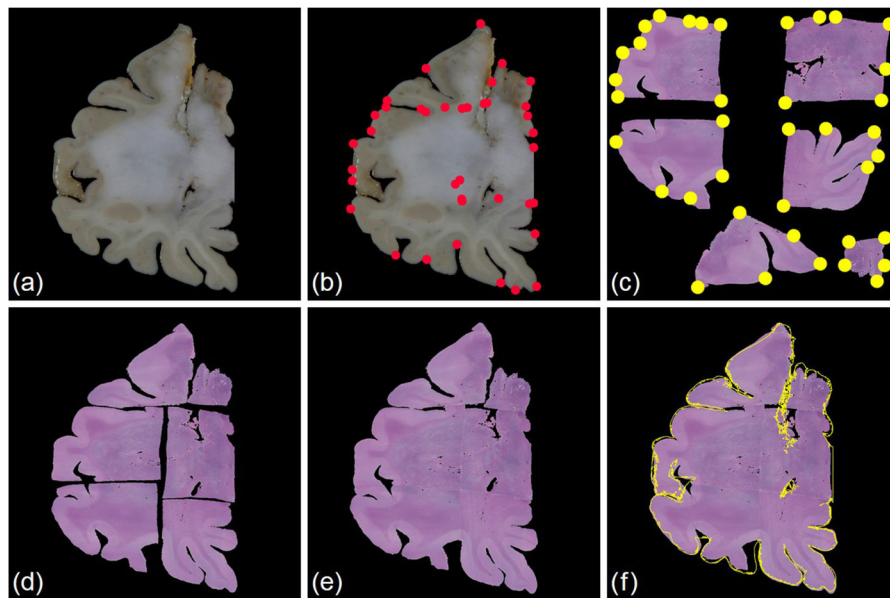
Fig. 6.

Results of OM–PT image registration with the connection step for the left part of the second gross section. (a) OM image of the left part of the second gross section; (b) OM image with selected target points; (c) PT images with selected control points before OM–PT image registration; (d) aligned PT images after OM–PT image registration; (e) connected PT image; (f) superimposed image with (e) and edge of (a). Red dots represent target points; yellow dots represent control points. (For interpretation of the references to colour in this figure legend, the reader is referred to the web version of this article.)

Fig. 7.
Results of OM–PT image registration with the connection step for the right part of the second gross section. (a) OM image of the right part of the second gross section; (b) OM image with selected target points; (c) PT images with selected control points before OM–PT image registration; (d) aligned PT images after OM–PT image registration; (e) connected PT image; (f) superimposed image with (e) and edge of (a). Red dots represent target points; yellow dots represent control points. (For interpretation of the references to colour in this figure legend, the reader is referred to the web version of this article.)
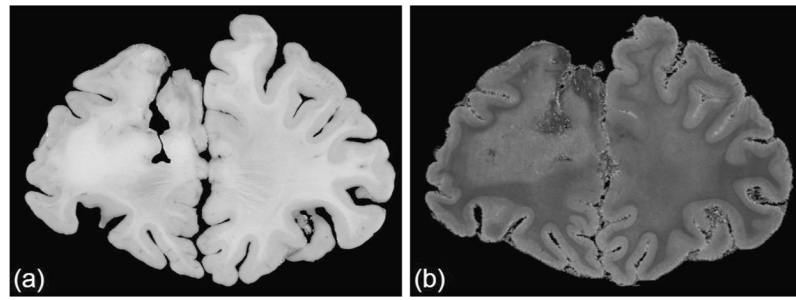
Fig. 8.
Results of OM–MR image registration for the first gross section. (a) OM image of the green channel; (b) optimized cross-sectional MR image. (For interpretation of the references to colour in this figure legend, the reader is referred to the web version of this article.)
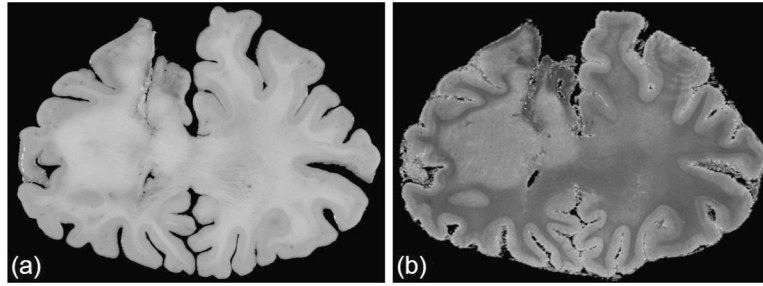
Fig. 9.
Results of OM–MR image registration for the second gross section. (a) OM image of the green channel; (b) optimized cross-sectional MR image. (For interpretation of the references to colour in this figure legend, the reader is referred to the web version of this article.)
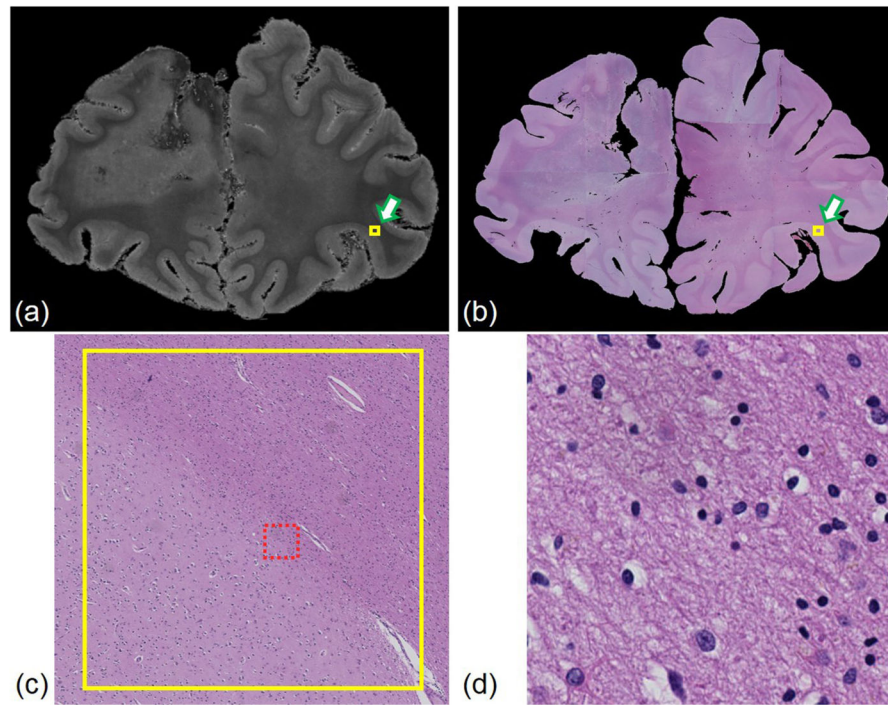
Fig. 10.
Results of searching for corresponding regions using conversion parameters obtained with the proposed method. (a) Extracted cross-sectional MR image; (b) connected PT image; (c) enlarged PT image around the solid yellow square in (b); (d) enlarged PT image for the dotted red square in (c). (For interpretation of the references to colour in this figure legend, the reader is referred to the web version of this article.)
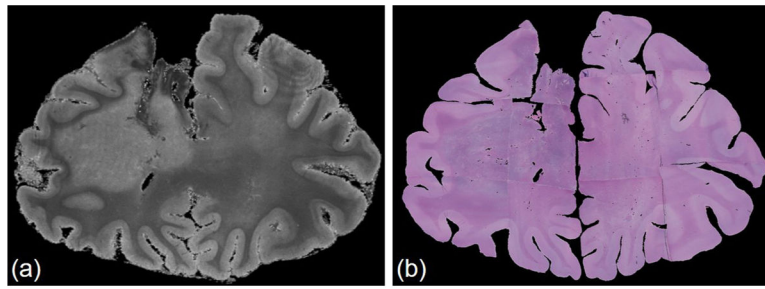
Fig. 11.
Results of the proposed method for the second gross section. (a) Extracted cross-sectional MR image; (b) connected PT image.